Outstanding conversion efficiency of 38.39% from a Perovskite/CIGS tandem PV cell: A synergic optimization through computational modeling

Md Ashraful Islam [a], Atik Jawad [b], Nahid Akhter Jahan [a], M. Mofazzal Hossain [b,*]

[a] *Department of Electrical and Electronic Engineering, Southeast University, Dhaka-1212, Bangladesh*
[b] *Department of Electrical and Electronic Engineering, University of Liberal Arts Bangladesh, Dhaka-1207, Bangladesh*

A B S T R A C T

An all-inorganic lead-free tandem PV cell consisting of two sub-cells $CsSn_{0.5}Ge_{0.5}I_3$ (perovskite) based top cell/CIGS-based bottom cell has been designed, simulated, and optimized by varying the thickness of pertinent layers utilizing the SCAPS-1D simulator. In the top sub-cell, a wide bandgap lead-free inorganic $CsSn_{0.5}Ge_{0.5}I_3$ perovskite is inserted as the primary absorber layer because of its distinctive characteristics with an ETL of ZnO, which is recognized for its high electron mobility & absorption coefficient, and an HTL of NiO to offer increased hole mobility with good chemical-durability. For the bottom sub-cell, we have selected p-type CIGS as the absorber with Spiro-OMeTAD as the apposite HTL to provide suitable offsets of valence and conduction band distribution and TiO_2 as ETL to offer low-cost, low-ecotoxicity, excellent optical properties, and chemical-stability and thus offers improved efficiency of the overall tandem structure. In the beginning, the two sub-cells were simulated independently; the top sub-cell was simulated under the standard spectrum of AM1.5G, while the bottom sub-cell was optimized using a filtered spectrum. Thereafter, the current matching point of both cells was attained by optimizing the absorber layer thicknesses. Finally, our computational modeling and simulation results offer the optimized cell structure revealing an outstanding overall 38.39% power conversion efficiency (*PCE*), Fill Factor (*FF*) of 83.4%, open-circuit voltage (V_{OC}) of 2.48 V, and short-circuit current density (J_{sc}) of 18.64 mA cm^{-2}. The proposed tandem structure's performance matrices outperform those stated in the most recent literature. These outcomes of the proposed structure are expected to facilitate the development and production of a low-cost and highly effective inorganic perovskite Tandem PV cell in the future.

1. Introduction

The world is constantly grappling with climate change owing to the deadly greenhouse gas emission and air pollutants resulting from fossil fuel-based combustion in generating electricity. Researchers worldwide have been endeavoring for decades to develop sustainable, environment-friendly, and cost-effective materials with suitable optoelectronic properties. Solar energy has become a popular renewable energy source due to its plenteous & environmentally friendly nature. The only direct means of converting solar radiation into electricity is through photovoltaic (PV) technology, which has gained widespread acceptance as one of the leading

potentials amidst sustainable & ecologocal energy-producing technologies complying with environmental, health, and safety requirements [1–3]. The price of PV manufacturing is largely determined by the price of constituents and power conversion efficiency (PCE). Note that, the main obstacles preventing the generation of power from photovoltaic-based technologies are PCE and the high cost of materials [4]. Therefore, the PV researchers are coming forward with various new concepts of solar-cell designs and formation valuing the climate issues, cost, stability, and efficacy in terms of commercial production. Namely, amorphous silicon, copper-indium-gallium-selenide (CIGS), cadmium telluride solar cell are classically been recognized as prospective candidates for PV-based electricity generation [4–7]. Among them, silicon-based PVs have been mostly controlling the present marketplace (almost 90%). Yet, the stagnated conversion efficiency (~25%) of Si technologies puts a barrier to the further growth of PV technologies [8]. After Si, CIGS-based solar cells have attracted a lot of attention because to their superior performance and lower cost compared to typical silicon-based solar cells. The chalcogenide semiconductor material known as CIGS is made up of the atoms of copper, indium, gallium, and selenium arranged in a crystal lattice. CIGS solar cells now have a record efficiency of 23.35% [9] and is commercially available. Nevertheless, the PCE of single-junction CIGS solar cells is limited owing to it's inability to capture a wider range of the solar insolation.

On the other hand, in both research and business, perovskite solar cells are emerging as a potential contender for achieving excellent efficiency and low-cost fabrication owing to their suitable optoelectronic properties including high absorption coefficient in the visible band, relatively high carrier mobility, and tunable energy bandgap. It is popularly expressed with the chemical formula ABX_3, where A is a monovalent cation (such as $CH_3NH_3^+$, $CH_3(NH_2)_2^+$, Cs, Rb), B is a divalent cation metal (such as Pb_2^+, Sn_2^+, or Ge_2^+), and X is a halide monovalent anion (for instance Cl^-, I^-, Br^-). These solar cells have thus far attained an outstanding efficiency of 25.7% [9]. Particularly, the low-price and environmentally plentiful organic lead-halide perovskite-based PV started to flourish in 2009 due to its rapid increase of PCE [9–15]. The deposition methods used for such perovskite layer range from spin-coating, sequential deposition, vacuum deposition, and spray pyrolysis. Despite their appealing PCE and simple production method, organic perovskite solar PVs hold the drawback of containing hazardous lead (Pb) as a basic ingredient and unsteady organic cations that are prone to continuous contact to radiation and moistness [15–17]. To mitigate the ecotoxicity and to circumvent these drawbacks, researchers have started to give attention to the toxic-free, inorganic substitute for lead as the key solar cell absorber layer [18–22]. By this time, inorganic perovskite has started gaining recognition owing to its rationally superior thermal stability in comparison to the organic equivalents. Out of the feasible selections for A, Cs^+ is considered a suitable alternative to organic cations like $CH_3NH_3^+$ and $CH_3(NH_2)_2^+$. This $CsBX_3$ is recognized as a satisfactory composition because of its high absorption coefficient, great motility of carriers, well-balanced electron and hole diffusion lengths, better defect endurance, small binding energy of electron-hole, and tunable bandgap making it one of the appropriate selections for tandem PV cells [23–31]. For instance, $CsGeI_3$, $CsSnI_3$, and $CsSnBr_3$ are the recently encountered most popular lead-free inorganic $CsBX_3$ compounds for solar cell fabrication. It is worth mentioning that lead (Pb) replacement by Sn and Ge is quite viable and suitable for wholesale production mostly attributed to the suitable absorption coefficient ($>10^5$ cm^{-1}), the lengthier state of oxidation of tin, suitable bandgap (1.2–1.7 eV) and acceptable moistness stability [24–31] and thus attains favorable PCE [31]. Recently a numerical investigation reveals the performance of $CsGeI_3$ perovskites with 18.30% of simulated PCE [31]. Recently Hossain et al. reported an efficiency of 19.06% from a $CsPbI_3$-based inorganic perovskite solar cell using numerical simulation [32]. Similarly, conducting numerical simulation using SCAPS-1D simulator, Islam et al. investigated the photovoltaic performance of $TiO_2/Cs_2SnI_6/SrCu_2O_2$ and reported an efficiency of 32.72% [33]. At the same time, research on tandem based solar cell design is gaining attention in terms of achieving the highest possible PCE overcoming the Shockley-Queisser limit. In tandem solar cells, two or more solar cells with different bandgaps are generally connected in series, allowing for better absorption of the solar spectrum. High-energy photons are absorbed by the top cell, which has a bigger bandgap, while low-energy photons are absorbed by the bottom cell, which has a smaller bandgap. The complementing absorption spectra of the two materials can be used to increase the efficiency of tandem solar cells made of perovskite and CIGS. The efficiency of tandem perovskite-CIGS solar cells has reached a record high of 23.26% [34], surpassing the efficiency of single-junction CIGS solar cells. Several strategies have been proposed to improve the performance and stability of tandem perovskite-CIGS solar cells. One approach is the optimization of the bandgap of the perovskite and CIGS layers to achieve better spectral matching. It involves the deposition of the inorganic perovskite on top of a pre-existing CIGS cell. The perovskite cell functions as the top cell in this arrangement, absorbing photons with energy above its bandgap while the bottom cell, the CIGS cell, does the opposite. Another approach is to employ a graded bandgap design, where the bandgap of the perovskite and CIGS layers are gradually varied to improve light absorption and reduce the current mismatch. Encapsulation of the perovskite layer with a protective layer has also been proposed to improve the stability of tandem perovskite-CIGS solar cells [35].

Several existing works have reported the use of different perovskite materials, including $CsPbI_3$, $CsPbBr_3$, and $CsPb(Cl/Br)_3$, in tandem solar cells with CIGS [36]. A PCE of up to 22.4% has been reported for an inorganic-organic hybrid perovskite-CIGS tandem solar cell, which is higher than the PCEs of individual perovskite and CIGS cells [37]. The highest reported efficiency for a perovskite-CIGS tandem solar cell with a fully scalable architecture is 24.2% [35]. However, they all include toxic lead.

A perovskite absorber layer is typically embedded between an ETL and an HTL in a perovskite based sub-cell device. The inclusion of ETL/HTL in the perovskite sub-cell is essential for taking out the photo-generated electron-hole pairs from the absorber layer (perovskite) to the outer contacts. A right selection of ETL and HTL is often a must for active separation of carriers mostly due to the suitable energy band alignments; the electron transport layer assists conducting electrons while ceasing the holes and the hole transport layer helps hole-conduction by ceasing electrons. The popular choice of ETL materials in perovskite solar cells are Fe_2O_3, SnO_2, ZnO, ZnOS, TiO_2, In_2O_3, PCBM, and amorphous $InGaZnO_4$ (a-IGZO) [38–45]. Among these ETLs, ZnO offers excellent electronic properties e.g., good stability, easy to fabricate, low cost, non-toxic and eco-friendly features. Similarly, TiO_2 is considered as one of the most common and frequently used ETLs for its suitable features such as enhanced electron mobility, lesser ecotoxicity and lastingness,

and low cost. Furthermore, both organic (for instance, PEDOT: PSS, Spiro-OMeTAD, P3HT, PTAA) and inorganic (for instance, NiO, CZTSe, Cu$_2$O, CuSCN, CuI, and CuO$_x$) materials are proposed as suitable materials for HTL to improve overall performance and durability [46–50]. Perovskite cells having such HTLs have been reported to achieve PCE up to 19.82% so far [49].

According to recent research, the low PCE of tandem perovskite solar cells is likely caused by both the non-radiative recombination of excitons in the bulk and the increased carrier capture areas in interfacial defects (such as absorber-ETL and absorber-HTL interfaces as well as sub-cell boundaries or buffer layers). Energy-band alignments, proper thickness of each absorber layer, and defects at boundaries are the major determining factors of achieving short-circuit current matching among the sub-cells connected in series. Therefore, in-depth research is indispensable to understand the carrier dynamics throughout the entire solar cell architecture and their
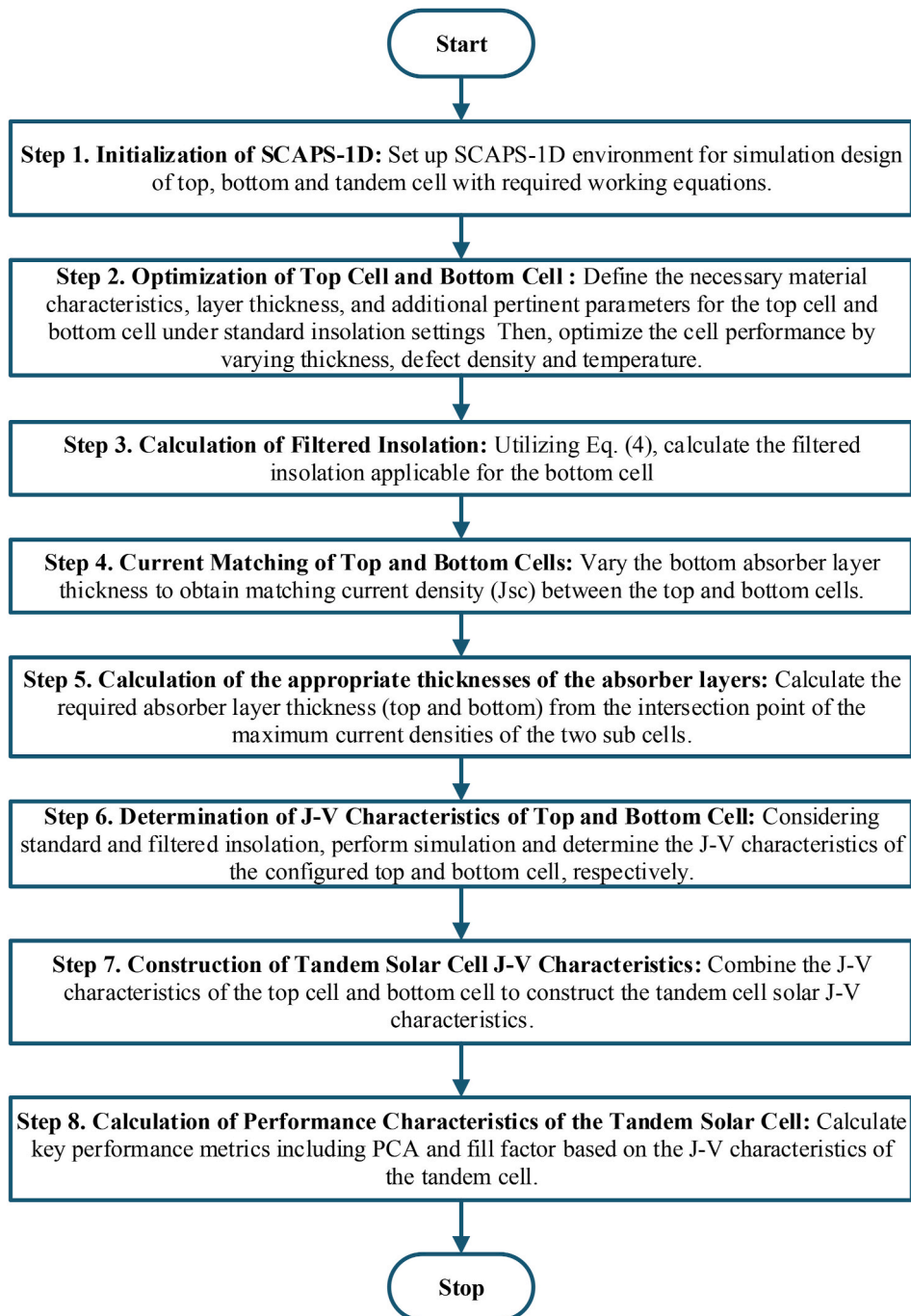
```
┌─────────────┐
│    Start    │
└─────────────┘
       │
       ▼
┌──────────────────────────────────────────────────────┐
│ Step 1. Initialization of SCAPS-1D: Set up SCAPS-1D   │
│ environment for simulation design of top, bottom and  │
│ tandem cell with required working equations.           │
└──────────────────────────────────────────────────────┘
       │
       ▼
┌──────────────────────────────────────────────────────┐
│ Step 2. Optimization of Top Cell and Bottom Cell:     │
│ Define the necessary material characteristics, layer  │
│ thickness, and additional pertinent parameters for    │
│ the top cell and bottom cell under standard insolation│
│ settings  Then, optimize the cell performance by      │
│ varying thickness, defect density and temperature.    │
└──────────────────────────────────────────────────────┘
       │
       ▼
┌──────────────────────────────────────────────────────┐
│ Step 3. Calculation of Filtered Insolation: Utilizing │
│ Eq. (4), calculate the filtered insolation applicable │
│ for the bottom cell                                    │
└──────────────────────────────────────────────────────┘
       │
       ▼
┌──────────────────────────────────────────────────────┐
│ Step 4. Current Matching of Top and Bottom Cells:     │
│ Vary the bottom absorber layer thickness to obtain    │
│ matching current density (Jsc) between the top and    │
│ bottom cells.                                          │
└──────────────────────────────────────────────────────┘
       │
       ▼
┌──────────────────────────────────────────────────────┐
│ Step 5. Calculation of the appropriate thicknesses of │
│ the absorber layers: Calculate the required absorber  │
│ layer thickness (top and bottom) from the intersection│
│ point of the maximum current densities of the two sub │
│ cells.                                                 │
└──────────────────────────────────────────────────────┘
       │
       ▼
┌──────────────────────────────────────────────────────┐
│ Step 6. Determination of J-V Characteristics of Top   │
│ and Bottom Cell: Considering standard and filtered    │
│ insolation, perform simulation and determine the J-V  │
│ characteristics of the configured top and bottom      │
│ cell, respectively.                                    │
└──────────────────────────────────────────────────────┘
       │
       ▼
┌──────────────────────────────────────────────────────┐
│ Step 7. Construction of Tandem Solar Cell J-V         │
│ Characteristics: Combine the J-V characteristics of   │
│ the top cell and bottom cell to construct the tandem  │
│ cell solar J-V characteristics.                        │
└──────────────────────────────────────────────────────┘
       │
       ▼
┌──────────────────────────────────────────────────────┐
│ Step 8. Calculation of Performance Characteristics of │
│ the Tandem Solar Cell: Calculate key performance      │
│ metrics including PCA and fill factor based on the    │
│ J-V characteristics of the tandem cell.                │
└──────────────────────────────────────────────────────┘
       │
       ▼
┌─────────────┐
│    Stop     │
└─────────────┘
```

Fig. 1. The proposed methodology of designing tandem solar cell.

fabrication process for large-scale commercialization of lead-free tandem perovskite-CIGS solar cells through synergic optimization of the absorber layers of the two sub-cells and their interface.

In this research, we have taken the above observations into account and focused on conducting a thorough computational modeling of a novel tandem (two sub-cells) $CsGe_{0.5}Sn_{0.5}I_3$ (top sub-cell)–CIGS (bottom-sub-cell) solar cell structure utilizing SCAPS-1D simulator. The main objective of this work is to find an efficient combination of non-toxic solar cells with high efficiency so that it saves time and effort before going for fabrication. The uniqueness & novelties of the proposed structure are: (i) The structure is all-inorganic and it is better than the organic equivalents that are susceptible to uninterrupted exposure to radiation, heat, and humidity. (ii) It is completely lead-free and therefore non-toxic. (iii) We envisioned designing a tandem architecture by overcoming the limitation of the SCAPS-1D simulator that typically cannot compute devices with more than 7-layers. Briefly, a comprehensive methodology is proposed to construct tandem cell by leveraging the characteristics of separately optimized bottom and top cells in SCAPS-1D. The steps associated with the designing are generalized, thus, the proposed method is applicable for tandem cells composed of other materials too. Throughout, we have shown that two individual sub-cells are simulated separately where the structural parameters are collectively optimized to attain the highest possible PCE. We have also explored the most suitable ETL and HTL materials for the maximum possible PCE in the individual sub-cells. Afterward using a filtered spectrum (calculated using MATLAB), desired current matching condition was achieved for the overall series connected cells. This approach headed to the desired highest PCE of our tandem structure. We surmise that this research will aid the researchers in the simulation-based solar-cell research field, considering the optimization of the multi-junction solar cells using this simple SCAPS-1D simulator before experimental exploration.

2. Proposed design methodology

This section describes the methodology of designing the proposed perovskite/CIGS-based tandem solar cell in SCAPS-1D. The steps associated with the full procedure are outlined below. Moreover, a detailed flowchart showing all the steps of the design is given in Fig. 1.

Step 1.   Initialization of SCAPS-1D: In this research work, the software SCAPS-1D, developed by Prof. M. Burgelman [51] is utilized for the solar cell simulation design. It is a sophisticated software application that provides a comprehensive suite of tools for assessing and improving the performance of solar cells and modules. It uses advanced algorithms and models for predicting the electrical characteristics of photovoltaic devices under varying environmental conditions and operating scenarios. With its broad range of features and capabilities, SCAPS-1D is a widely utilized software for the analysis of solar cells [5],[13],[14],[20],[23],[32],[51].

The PV cell is modeled in this software as a stack of layers, where each layer's thickness, doping, and other physical properties of the materials that make it up are specified. It solves three differentially coupled equations (Eqs. (1)–(3)) for calculating the performance matrices of the designed cells. Here, Eq. (1) represents Poisson's equation, and Eqs. (2) and (3) represent the electron and hole continuity equations [51,52].

$$\frac{\partial^2 \psi}{\partial x^2} + \frac{q}{\varepsilon}\left[p(x) - n(x) + N_D - N_A + \rho_p - \rho_n\right] = 0 \tag{1}$$

$$\frac{\partial J_P}{\partial x} = -G(x) + R(x) \tag{2}$$

$$\frac{1}{q}\frac{\partial J_n}{\partial x} = G(x) - R(x) \tag{3}$$

The software solves these equations concurrently and determines the characteristics of the solar cells. In Eqs. (2) and (3), $R(x)$ represents the recombination rate which includes the Shockley–Read–Hall (S-R-H) recombination and Auger recombination, for this particular work. To start the simulation process, first, SCAPS-1D software environment is set up for designing the top and bottom cells of the proposed tandem cell.

Step 2.   **Optimization of Top and Bottom Cell:** After setting up the SCAPS -1D environment, we intended for the simulation of two

Table 1
Electrical parameters for the materials of top cell and bottom cell.

Electrical Parameters	Bottom Cell				Top Cell			
	FTO	TiO$_2$	P-CIGS	Spiro-OMETAD	ITO	ZnO	CsSn$_{0.5}$Ge$_{0.5}$I$_3$	NiO
E_g (eV)	3.5	3.26	1.100	2.9	3.6	3.37	1.50	3.6
χ (eV)	4.0	4.2	4.5	2.2	4.1	4.35	3.90	1.8
ε	–	10.0	28.0	13.6	10	11.70	9.00	3.0
N_C (cm^{-3})	2.2×10^{18}	2.2×10^{18}	2.2×10^{18}	2.2×10^{18}	2.2×10^{18}	2.2×10^{18}	1.0×10^{19}	2.5×10^{20}
N_V (cm^{-3})	1.8×10^{18}	1.8×10^{18}	1.8×10^{19}	1.6×10^{19}	1.8×10^{18}	1.78×10^{19}	1.0×10^{19}	2.5×10^{20}
μ_n (cm^2/Vs)	20.0	20.0	100.0	1.0×10^{-4}	50.0	100.0	9.74×10^2	2.8
μ_p (cm^2/V.s)	10.0	10.0	25.0	1.0×10^{-4}	75.0	50.0	2.13×10^2	2.8
N_D (cm^{-3})	1.0×10^{22}	1.0×10^{22}	0	0	1.0×10^{22}	1.0×10^{22}	0	0
N_A (cm^{-3})	0	0	1.0×10^{22}	1.0×10^{22}	3.6	0	1.0×10^{22}	1.0×10^{22}

sub-cells separately. One cell is proposed as the top cell, and the other one is proposed as the bottom cell. While conducting individual cell simulations, pertinent material parameters were given as inputs in the layered architecture (the values were taken from existing literature [13,14,20,23,53]). Thereafter, the thicknesses of each layer, and the doping concentrations of the absorber layer, ETL, and HTL layer were optimized utilizing the Batch Calculation features of the simulator to attain the highest possible figure of merits for both cells separately.

It is worth noting that, the top cell of the tandem cell is crucially important to the functioning of the entire cell in terms of absorbing high-energy photons. The proposed top solar cell comprises an FTO (transparent conducting layer), a ZnO (electron transport layer), a $CsSn_{0.5}Ge_{0.5}I_3$ (high-band gap energy absorber layer), and a NiO (hole transport layer); all collaborate to produce an efficient and effective means of absorption of light, separation of charge, and transport. The details of the taken materials' properties are outlined in Table 1. The initial calibration with the selected combination is conducted in this step at standard AM1.5G spectrum to configure the top cell properly.

Similarly, the bottom cell is constructed in SCAPS-1D with ITO (transparent conducting oxide layer), TiO_2 (electron transport layer), P-CIGs (energy absorber layer of high-band gap), and Spiro-OMETAD (hole transport layer).

By stacking two cells on top of one another, the tandem cell has been constructed for maximum utilization of the solar spectrum and improving total PCE. In this work, CIGS is chosen as the bottom absorber layer and $CsSn_{0.5}Ge_{0.5}I_3$ as the top cell absorber layer. With this pairing, a wider percentage of the solar spectrum can be utilized since CIGS has a low band gap energy (1.0–1.7 eV) and $CsSn_{0.5}Ge_{0.5}I_3$ has a high band gap energy (1.5–2.0 eV). Because of the inorganic perovskite layer, this combination is also economical and environmentally friendly [54]. Furthermore, this tandem structure is more stable due to the bottom cell's protection and the greater stability of the perovskite layer. The chosen parameters for conducting cell calibration at standard AM1.5G spectrum are given in Table 1. The properties of all necessary design parameters needed for simulation have been collected from existing established literature [13,14,20,23,33,53].

Step 3. Calculation of Filtered Insolation: When two cells (top and bottom) are stacked to construct a tandem cell, a reverse-biased p-n junction develops at their interface, preventing current flow across the cell [55]. The current matching approach, which necessitates a tunnel recombination junction, is employed to ensure equal current flow in each sub-cell. The junction simulation, however, is not possible in SCAPS-1D due to software limitations. In light of this, separate simulations are run for each cell, taking into account a perfect tunnel recombination junction with no carrier losses [56–58]. To achieve that purpose, the top cell is simulated using the AM1.5G spectrum. After the sunlight has passed through the top cell, it illuminates the bottom cell using filtered insolation that is determined using Eq (4) [54].

$$S_f(\lambda) = S_o(\lambda) * exp\left(\sum_{j=1}^{3} -\alpha_{mat_i}(\lambda) * d_{mat_i}\right) \tag{4}$$

Here, $S_o(\lambda)$ represents the AM 1.5G standard insolation, $S_f(\lambda)$ denotes the filtered insolation that transmits through the top cell, $\alpha_{mat_i}(\lambda)$ and d_{mat_i} represents the absorption coefficient and thickness of the ith material of the top cell, respectively. In this work, the three materials of the top cell (i = 1, 2, and 3) correspond to ZnO, perovskite, and NiO, respectively. For several thicknesses of the top cell absorber layer (100 nm–1000 nm), filtered insolation has been calculated using MATLAB to obtain the desired current matching purpose explained in the next step.

Step 4. **Current Matching of Top and Bottom Cells:** The current matching of both sub-cells is conducted to ensure uniform current flow in the proposed tandem cell in this step. Thickness increases beyond the threshold value resulting in increased absorption in the top sub-cell and decreased optical coupling in the bottom cell. Current density in tandem cells decreases with decreased coupling and vice versa. To achieve an identical short circuit current (J_{sc}), the thickness of the sub-cells (top and bottom) in tandem structure is modified. To do this, the bottom absorber layer's thickness is changed from its starting value (100 nm) to its final value (1000 nm). Each bottom cell thickness scenario receives the filtered insolation determined in the preceding step for various top layer thicknesses. The value of associated current density (J_{sc}) for each scenario is then noted. Finally, the J_{sc} of all the simulated bottom layer and top layer thicknesses are plotted against top cell thickness. The current matching values for different layer thicknesses are obtained from the plot intersection points.

Step 5. **Calculation of the Required Absorber Layers Thicknesses:** After the intersection points are identified from the J_{sc} vs top layer thickness plot, the most appropriate value of thickness is chosen. Note that, increased current density results in increased output power from the tandem cell, i.e., increased overall power conversion efficiency (PCA) as well. Consequently, the criterion for the best choice of thickness is to choose the combination that results in the maximum J_{sc} out of all the possible combinations. After identifying the maximum current density intersection point, the corresponding top and bottom layer thickness is chosen for the tandem cell.

Step 6. **Determination of J-V Characteristics of Top and Bottom Cell:** The constructed top and bottom cells with the chosen absorber layer thicknesses are exposed to insolation in this stage to determine their performance characteristics. It should be noted that the standard AM1.5G insolation is used for illuminating the top sub-cell. The filtered insolation associated with the specified top cell layer thickness is computed for the bottom sub-cell using Eq. (4), and then applied to the bottom cell to determine the current density (J_{sc}) against voltage (V) characteristics.

Step 7. **Construction of Tandem Solar Cell J-V Characteristics:** The J-V characteristic of the tandem cell can be derived by combining the J-V characteristics of the two sub-cells. This is accomplished by connecting the two cells in series so that the current

produced by the bottom cell passes through the top cell. In our study, recombination losses at the cell interface between the two cells are ignored, and the voltage produced by the tandem cell is equal to the total voltage produced by the individual sub-cells. The J-V characteristics of the proposed cell are therefore determined using the properties of the sub-cells calculated in the preceding steps.

Step 8. **Calculation of Performance Characteristics of the Tandem Solar Cell:** In the final step of the method, key performance indicators of the proposed tandem cell are determined. In addition to V_{OC} and J_{sc} two important indices, fill factor (*FF*) and PCE are calculated for the designed cell. In our research, these two crucial variables are assessed for the bottom, top, and tandem cells, and comparisons are made to determine how well the proposed tandem cell functions.

3. Results and analysis

The proposed tandem solar cell's simulation results and associated in-depth analysis are described in this part, using the suggested technique. The entire section is divided into a series of subsections that describe the steps and results of the entire method in order.

3.1. Optimization of top and bottom sub-cells

3.1.1. Structural details and energy band diagrams of top and bottom sub-cells

The present study presents a thorough investigation of the proposed structure for thin-film solar technology. The top and bottom cells of the structure are preliminarily optimized separately in standalone conditions to ensure proper working conditions and to obtain the highest performance parameters considering V_{OC}, J_{sc}, fill factor (*FF*), and efficiency. Before starting the initial simulation, all layers in the structure were set to be as thin as possible. The use of 20 nm thickness layers has been reported in the literature for experimental designs [59]. For this investigation, the parameters from Table 1 have been used for the preliminary simulation of both sub-cells in the current study. The thickness of each layer including the transparent conducting oxide layer and Electron/hole transport layers such as ITO, ZnO, and NiO in the top cell and FTO, TiO$_2$, and Spiro-OMETAD layers in the bottom cell were each selected as 30 nm. We observed that the thickness of the transparent conducting oxide layer and Electron/hole transport layers did not create any significant change in performance parameters when it was varied from 20 nm to 30 nm. In addition, we observed slightly increased efficiency for 30 nm of these layers on both sub-cells. Therefore, we selected 30 nm for those layers. Concerning the absorber layer, we started the simulation with 100 nm, as indicated in Table 2.

Thereafter, using the batch calculation feature of SCAP-1D we varied the thickness up to 1000 nm for both cells and observed an increase in efficiency with the increase of absorber thickness, which is atypical. [The thickness versus efficiency graph is discussed in the next section of the individual cell]. While configuring the two sub-cells in terms of thickness, we considered ZnO as ETL and NiO as HTL as the best matches for the absorber of the top cell; whereas TiO$_2$ as the ETL and Spiro-OMETAD as the HTL were the perfect matches for the bottom sub-cell. The proposed top and bottom cell structures are illuminated using standard AM 1.5G insolation, as illustrated in Fig. 2 (a) and **(b)**, respectively.

The performance of a PV cell is significantly impacted by the alignment of the energy levels. The energy band alignments of the two heterostructures (top sub-cell based on CsSn$_{0.5}$Ge$_{0.5}$I$_3$ and bottom sub-cell based on *p*-CIGS) are schematically portrayed in Fig. 3(a−b) in terms of the illustration of conduction-band minima and valence-band maxima, respectively. In both structures, a suitably uniform relationship between F_n and E_C; and between F_p and E_V, are perceived. Typically a PV structure is designed to provide a conducive band alignment so that holes can easily be transferred to the HTL while electrons can enter into the aligned conduction band of ETL effortlessly. Thereafter, the dissociated carriers are collected at the respective back-contacts and the transparent conducting layers. However, it is worth noting that, ETL should offer larger electron affinity higher than that of the absorber layer (such as CsSn$_{0.5}$Ge$_{0.5}$I$_3$ or P-CIGS) to attract the electrons efficiently at the ETL-absorber interface. Whereas, to extract the holes at the absorber-HTL interface, the HTL's ionization energy needs to be lower than the absorber layer's [23].

3.1.2. Effect of absorber thickness and its defect density on the performance of top and bottom cells

When light illuminates on the absorber layer of the perovskite, it generates excitons (electron-hole pairs), and thereafter contributes to the photo-current upon dissociation of excitons. However, the properties of the light-absorbing layer, such as thickness and the crystal regularity (uniformity) of this layer significantly influence the PCE of solar cell. The defect density of the absorber layer is a crucial aspect in determining the efficacy and therefore it directly affects the cell performance in a significant way. Besides, the defect states in the absorber and in its interfaces result in the intensification in the recombination of electron−hole, which abolishes the generated excitons and; ultimately cannot contribute to the photo-generated current. According to the previous works [20,23,28,32], the creation of pinholes and Shockley-Read-Hall non-radiative recombination are accountable for the decline in PV parameters and rise in absorber defect, which is one of the key reasons for carrier recombination, life-cycle reduction, and a weakening in the figure of merits of the solar cell.

Table 2
Selection of thicknesses of all layers of standalone top and bottom solar cells.

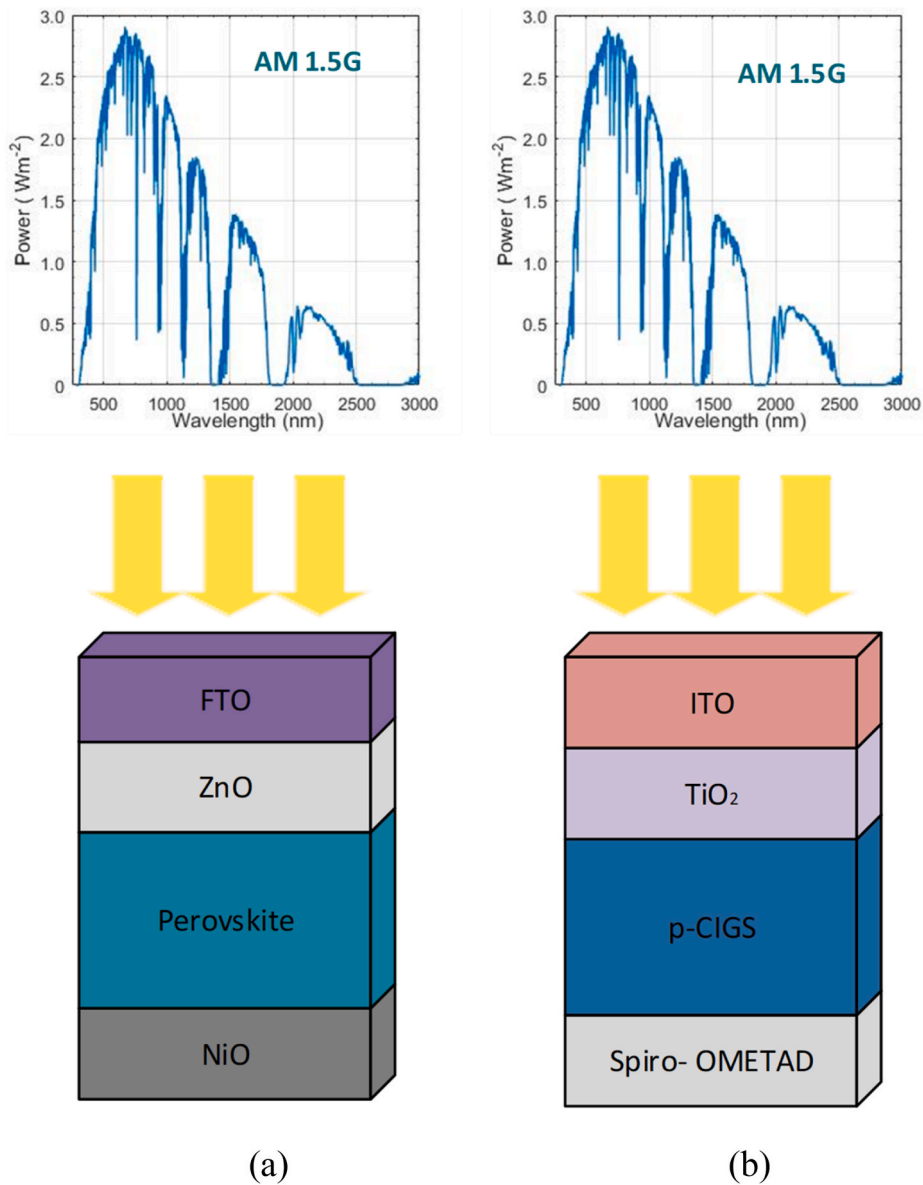|	Bottom Cell				Top Cell			
Material	FTO	TiO$_2$	P-CIGS	Spiro-OMETAD	ITO	ZnO	CsSn$_{0.5}$Ge$_{0.5}$I$_3$	NiO
Thickness (*nm*)	30	30	100–1000	30	30	30	100–1000	30

Fig. 2. The proposed top cell (a) and bottom cell (b) illuminated at standard 1.5G AM insolation.

At first, to identify the optimum thickness for the top sub-cell's absorber layer, the simulations were performed by varying the thickness of the absorber from 100 nm to 1000 nm (0.1–1.0 μm) shown in Fig. 4 (a), at a particular defect density of 10^{15} cm^{-3}. It is observed that the efficiency increases gradually from 100 nm to 1000 nm, almost starts to saturate at 800 nm, and then maximizes at 1000 nm with a value of 36.25%. Thereafter at a particular thickness of 800 nm, we investigated the optimum defect density for the structure (top sub-cell) by varying the defect density from 10^{10} to 10^{22} cm^{-3}, depicted in Fig. 4 (b). From the graph, we can see that the efficiency of the top cell decrease gradually (from 44.6% to 36%) when the defect density is varied from 10^{10} to 10^{15} cm^{-3}, then the efficiency further declines to 30% when the defect density rises up to 10^{17} cm^{-3}. The efficiency reduces to 20% of this top cell at the defect density of 10^{18} cm^{-3} and starts to decline significantly with the defect density beyond 10^{19} cm^{-3}.

Similarly, by increasing the absorber thickness from 100 nm to 1000 nm (0.1–1.0 μm), the simulation was employed to examine the impact of thickness on the absorber layer of the bottom sub-cell. shown in Fig. 5 (a), at the moderate defect density of 10^{15} cm^{-3}. Here, also, the efficiency escalates gradually from 100 nm to 1000 nm and maximizes at 1000 nm with a value of 32%.

Then, at a specific thickness of 1000 nm, we examine the structure (bottom sub-cell) by varying the defect density from 10^{10} to 10^{22} cm^{-3}, depicted in Fig. 5 (b). This figure presents that the efficiency of the bottom cell decrease gradually (from 44.3% to 32%) as the defect density is varied from 10^{10} to 10^{15} cm^{-3}, then efficiency further decreases to 28% when the defect density rises up to 10^{16} cm^{-3}. The efficiency shows linear declination after the defect density of 10^{17} cm^{-3}. The efficiency shrinks to 11% of this bottom cell at the
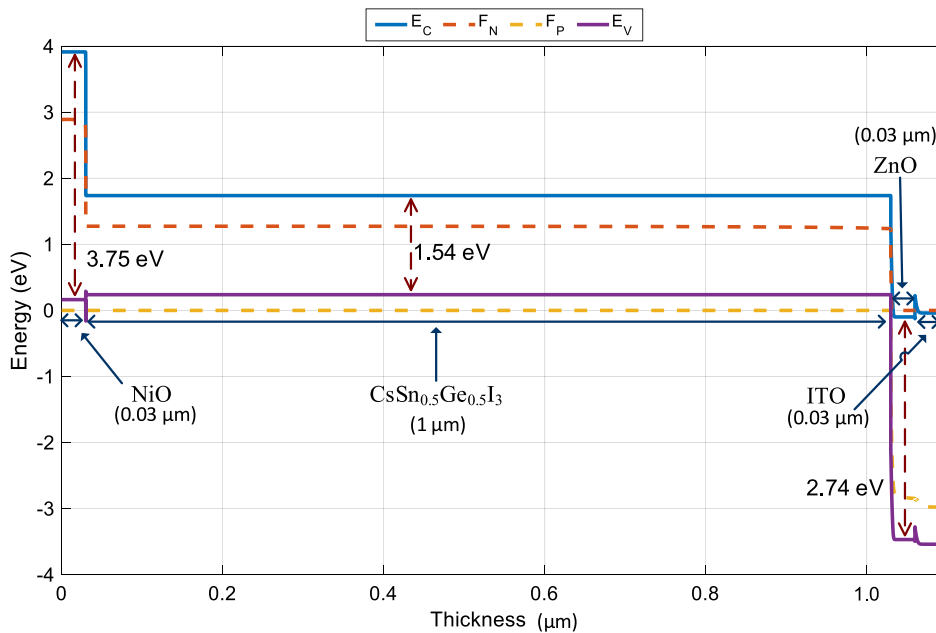
(a)
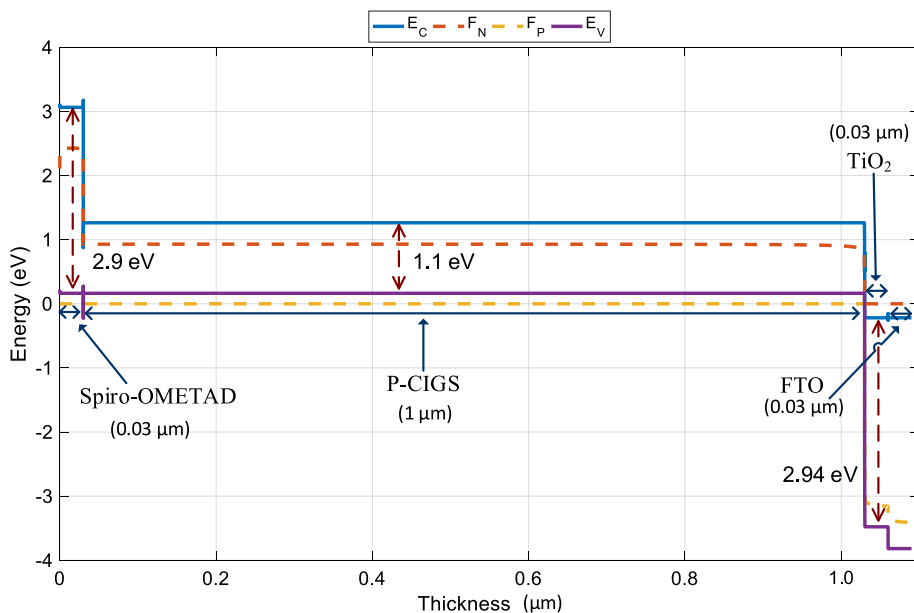
(b)

Fig. 3. Energy band diagram for (a) the top and (b) the bottom cell.

defect density of 10^{18} cm^{-3} and starts to decline considerably when the defect density exceeds 10^{19} cm^{-3}.

Comparing Figs. 4 (b) and Fig. 5 (b), it is apparent that the bottom cell is more defect prone than the top cell in terms of cell efficiency.

The effect of changing the absorber thickness and defect density on V_{OC}, J_{sc}, and FF of the top sub-cell is shown exemplarily in Fig. 6 as a contour plot. From Fig. 6 (a), it is observed that the thickness of the absorber layer has no major impact on the V_{OC} for a particular defect density. The structures show the maximum V_{OC} of around 1.79 V at the lowest defect density; and it shows a gradual decrement
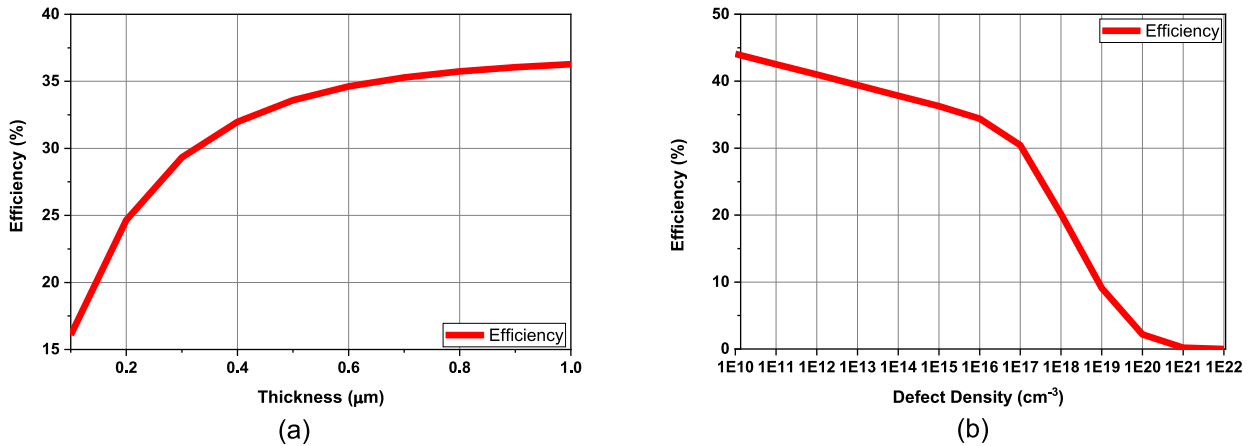
Fig. 4. The top cell optimization by varying (a) thickness, and (b) defect density, at standard AM1.5 G insolation.
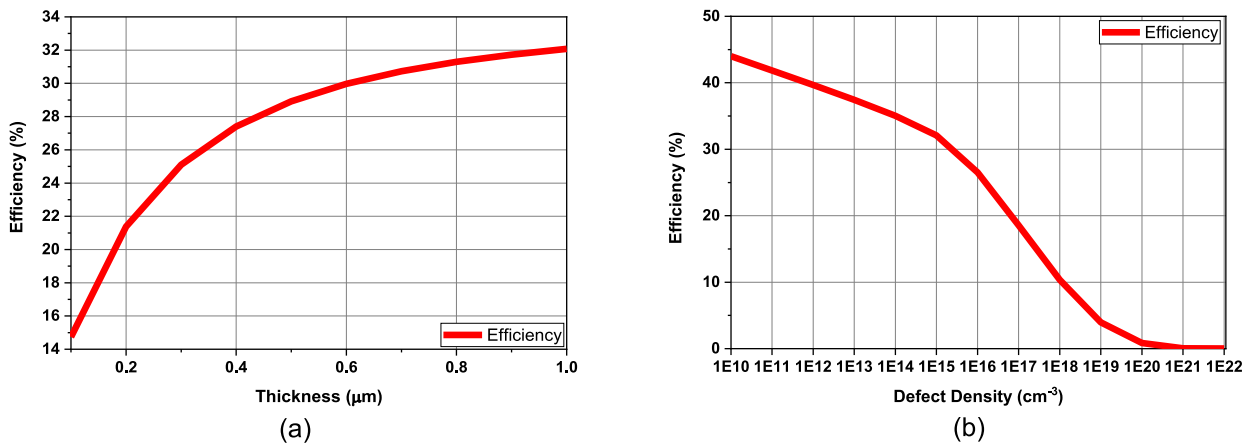
Fig. 5. Bottom cell optimization by varying (a) thickness, and (b) defect density, at standard AM1.5 G insolation.

of V_{OC} with the increase in defects. However, it shows quite acceptable V_{OC} of 1.44 V at a high defect density of 1×10^{17} cm^{-3}. Besides, this structure exhibits a reduction of V_{OC} from 1.44 to 1.09 V for an increase of defect densities from 1×10^{17} cm^{-3} to 1×10^{21} cm^{-3}. This indicates that the structure offers reasonably satisfactory V_{OC} of 1.09 V even at a much higher defect density of 1×10^{21} cm^{-3}. In parallel, from Fig. 6 (b) we notice that at a larger thickness J_{sc} increases significantly up to 27.9 mA/cm^2. It is also evident that beyond 10^{18} cm^{-3} of defect, the J_{sc} starts to decay even at larger thicknesses. In line with this, from Fig. 6 (c) it is found that the effect of the absorber thickness on the *FF* of this structure shows a similar trend as that of the V_{OC} (as shown in Fig. 6. (a)). It is apparent from the contour plot of Fig. 6 (c) that even at a much higher defect density of 10^{18} cm^{-3}, the *FF* offers an adequate value of 80.5%.

3.1.3. Effect of temperature on the PV performances of the sub-cells

Understanding PV performance at increased ambient temperatures is vital for anticipating the lifecycle of solar cells. It is very typical to cause performance fluctuations by overheat. Fig. 7 (a) & **(b)** portray the result of temperature fluctuations on the performance of our two sub-cells, respectively. It is apparent that the absorber is not much impacted by the temperature increase, which is consistent with the performance described in other publications [13,14,23]. The efficiencies are slightly sacrificed by only a few percentages with an increase of temperature even up to 400 K.

3.1.4. J-V characteristics of individually optimized top and bottom sub-cells

After the detailed analysis in terms of thickness, defect, and temperature, the corresponding *J-V* characteristics of the standalone top and bottom cells are illustrated in Fig. 8. The optimum V_{OC} values for the top and bottom cells are found as 1.4885 V and 1.0006 V, respectively. Furthermore, the corresponding current density magnitudes for the top and bottom cells are 18.67 mA/cm^2 and 36.012 mA/cm^2, respectively. The results show that the top cell offers a higher V_{OC} than the bottom cell. Regarding J_{sc}, the bottom cell yields a higher value. However, both cells show acceptable performance characteristics for standalone cells, making them useable for
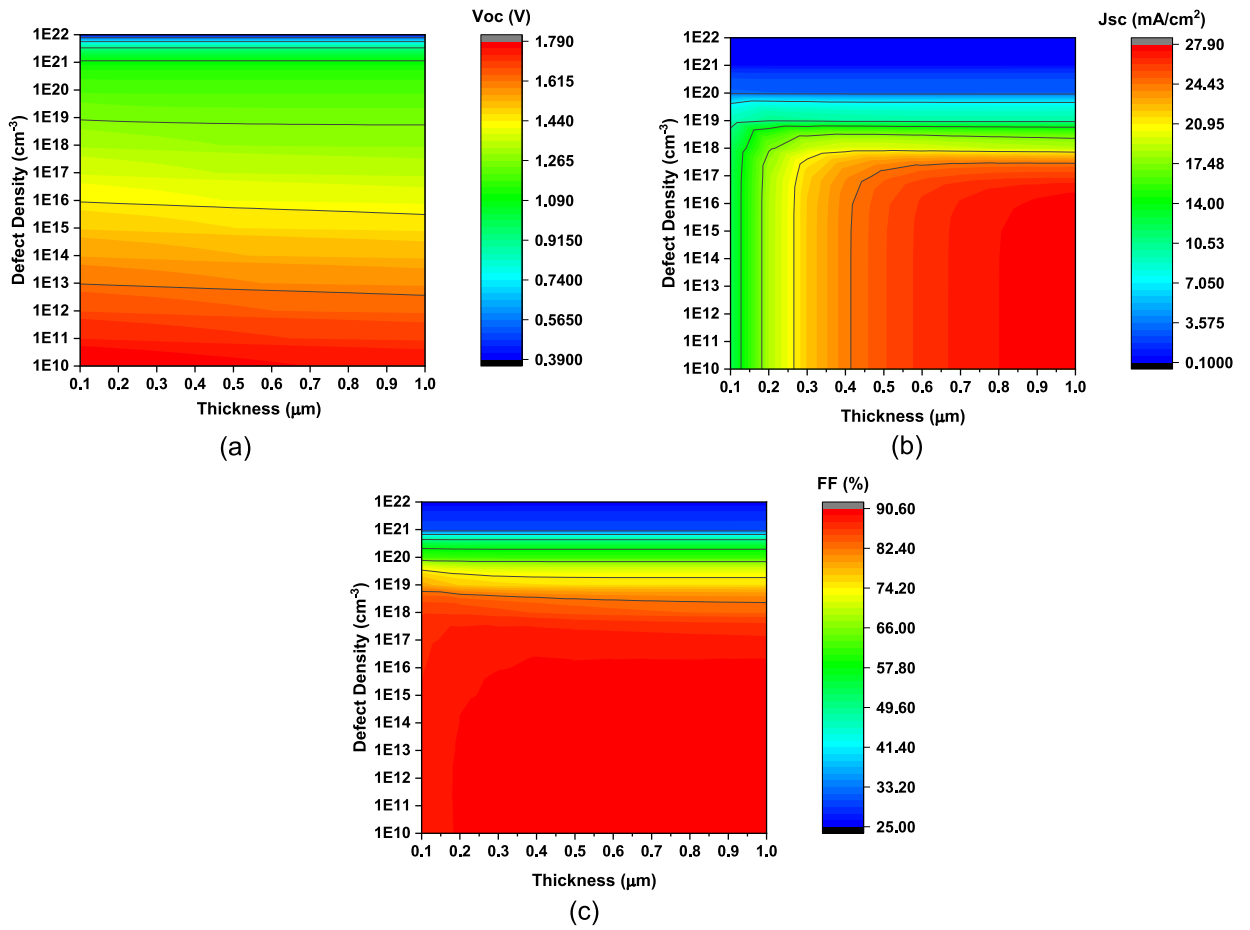
Fig. 6. Impacts of simultaneous variation of the top cell absorber layer thickness and defect density on (a) V_{OC}, (b) J_{sc}, and (c) *FF*.
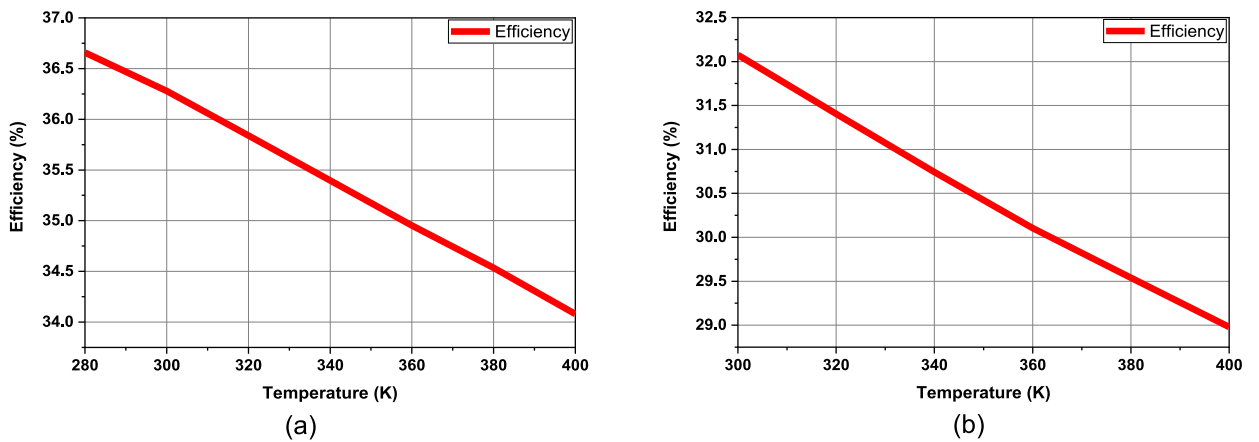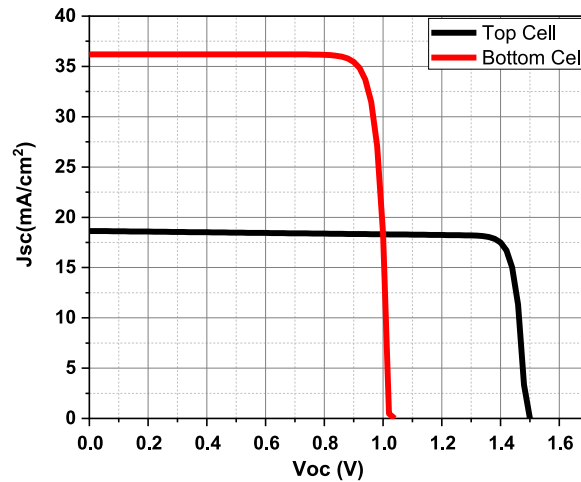

Fig. 7. Impact of temperature variation on the PV performances of the (a) top sub-cell and (b) bottom sub-cell.

Fig. 8. Standalone top and bottom cell's *J-V* characteristics after individual optimization at standard AM1.5 G insolation.

constructing tandem cell.

3.2. Filtered insolation identification

To properly allocate illumination for the bottom cell in the proposed tandem structure, the insolation transmitted through the top cell needs to be calculated first. The transmitted spectrum depends on layer material absorption coefficients and thickness, which are used to calculate filtered insolation. Utilizing Eq. (4), for various top absorber cell thicknesses from 100 nm to 1000 nm, the filtered insolation spectrums are determined. Total ten resultant filtered spectrums are illustrated with standard insolation in Fig. 9. Here, the pattern of the filtered insolation remains almost identical after each thickness but with decreasing spectrum strength as thickness increases. This is as a result of higher absorption in the top sub-cell's thick absorber layer. The amount of photocurrent absorbed in the top sub-cell varies depending on how thick or how thin the absorber layer is. The filtered insolation values are then used to match the current of both cells.

3.3. Current matching of top and bottom cells

As per the proposed methodology, the calculated filtered insolations for various top layer thicknesses are used for current density calculation for varying bottom layer thickness cells. The resulting current density with respect to varying absorber layer thickness is presented in Fig. 10. Note that, for an efficient tandem cell configuration, a higher matching current density is required. Analysis of the figure shows that the bottom layer's current density coincides with the top layer's current density at various points. However, the
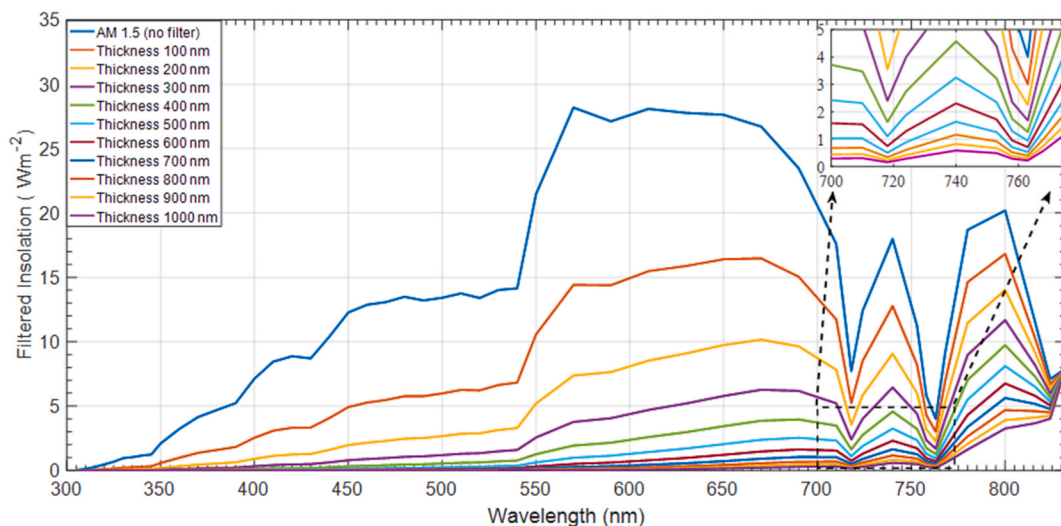
Fig. 9. Filtered insolation spectrum for varying top cell absorber layer thickness.
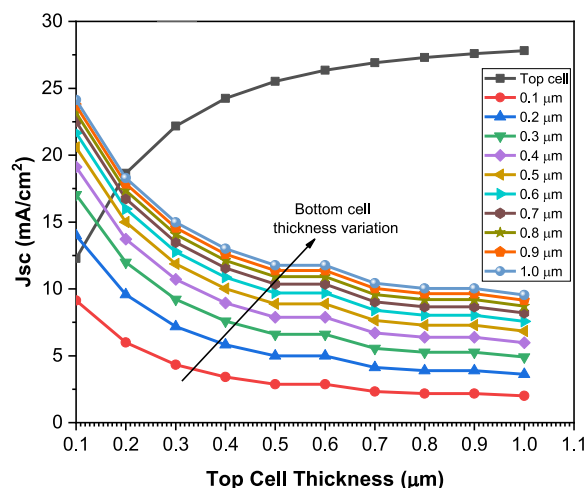
Fig. 10. Calculation of current matching by altering the thicknesses of the top and bottom absorber layers.

maximum current density at which both curves intersect is 18.64 mA/cm^2. This current density is achieved at a top absorber thickness of 198 nm and a bottom absorber thickness of 1000 nm. For tandem configuration, these two thicknesses for the absorber layers are chosen for getting the desired current matching performance.

3.4. Performance analysis of the entire tandem cell

To achieve the required absorber layer thicknesses, both sub-cells' absorber layers are modified as per the calculated values. The ZnO (30 nm)/Perovskite (198 nm)/NiO (30 nm) based top cell is re-illuminated at standard AM1.5G insolation. Using Eq. (4), the filtered insolation for the specific top cell thickness is computed for the bottom cell. The TiO$_2$ (30 nm)/p-CIGS (1000 nm)/Spiro-OMETAD (30 nm) based bottom cell is then illuminated with the filtered insolation spectrum. In this manner, the illumination of the proposed tandem cell at standard AM 1.5G is simulated. The detailed configuration and illumination setup are illustrated in Fig. 11.

In this work, we comprehensively investigate the J-V characteristics of the proposed tandem cell by first determining the J-V characteristics of both sub-cells individually, and then combining them serially to obtain the J-V characteristics of the tandem cell. Note that, to simulate the tandem cell characteristics, a perfect tunnel junction without carrier loss is assumed. The J-V characteristics of the tandem cell and the other sub-cells are illustrated in Fig. 12. For both sub-cells, the current density coincides at around 18.64 mA/cm^2, signifying the matching current. The results demonstrate that the voltage of the top cell (1.4885 V) and the bottom cell (1.0006 V) add up to yield a tandem cell voltage of 2.48 V, with the upper top cell dominating due to its relatively large V_{OC} value. Additionally, the current matches with the sub-cells at the same 18.64 mA/cm^2, underscoring the efficient tandem construction. Hence, the J-V characteristics of the proposed tandem cell are determined.

The result presents a comprehensive performance analysis of the calibrated individual sub-cells and the tandem cell, based on the evaluation of the *FF* and PCE. The maximum power points are identified from Fig. 12 to calculate the *FF* and PCE of each cell. The results show that the *FF* of the top cell, bottom cell, and proposed tandem cell are 89.077%, 86.282%, and 83.40%, respectively. Although the *FF* of the tandem cell has decreased slightly, it is well within acceptable limits. The tandem cell configuration exhibits a significant increase in the PCE, which rises to 38.39%, surpassing the previous PCEs of the top and bottom cells, which are 24.656% and 25.062%, respectively. This increase in efficiency amounts to approximately 13% and underscores the superior performance of the proposed tandem configuration. Table 3 contains an overview of the key characteristics of all the cells.

3.5. Comparison with previous work

Furthermore, this study is contrasted with several previous studies on Perovskite-CIGS-based tandem cells (both computational and experimental) to assess the performance of the proposed tandem solar cell. In Table 4, a detailed comparison of performance is provided. According to the findings of the analysis, the proposed structure exceeds the current works with a remarkable 38.39% PCE. In addition, a comparison of the other performance characteristics reveals acceptable results.

4. Conclusions

To increase the PCE and stability for commercial production in thin-film solar technology, an all-inorganic lead-free perovskite-CIGS tandem photovoltaic cell has been designed, simulated, and investigated in this work. The top sub-cell is proposed as ZnO/lead-free perovskite (CsSn$_{0.5}$Ge$_{0.5}$I$_3$)/NiO, while the bottom sub-cell is chosen as TiO$_2$/P-CIGS/Spiro-OMETAD. The two sub-cells (top and bottom) of the structure were initially optimized in standalone conditions. Then, by modeling the J-V curve of the bottom
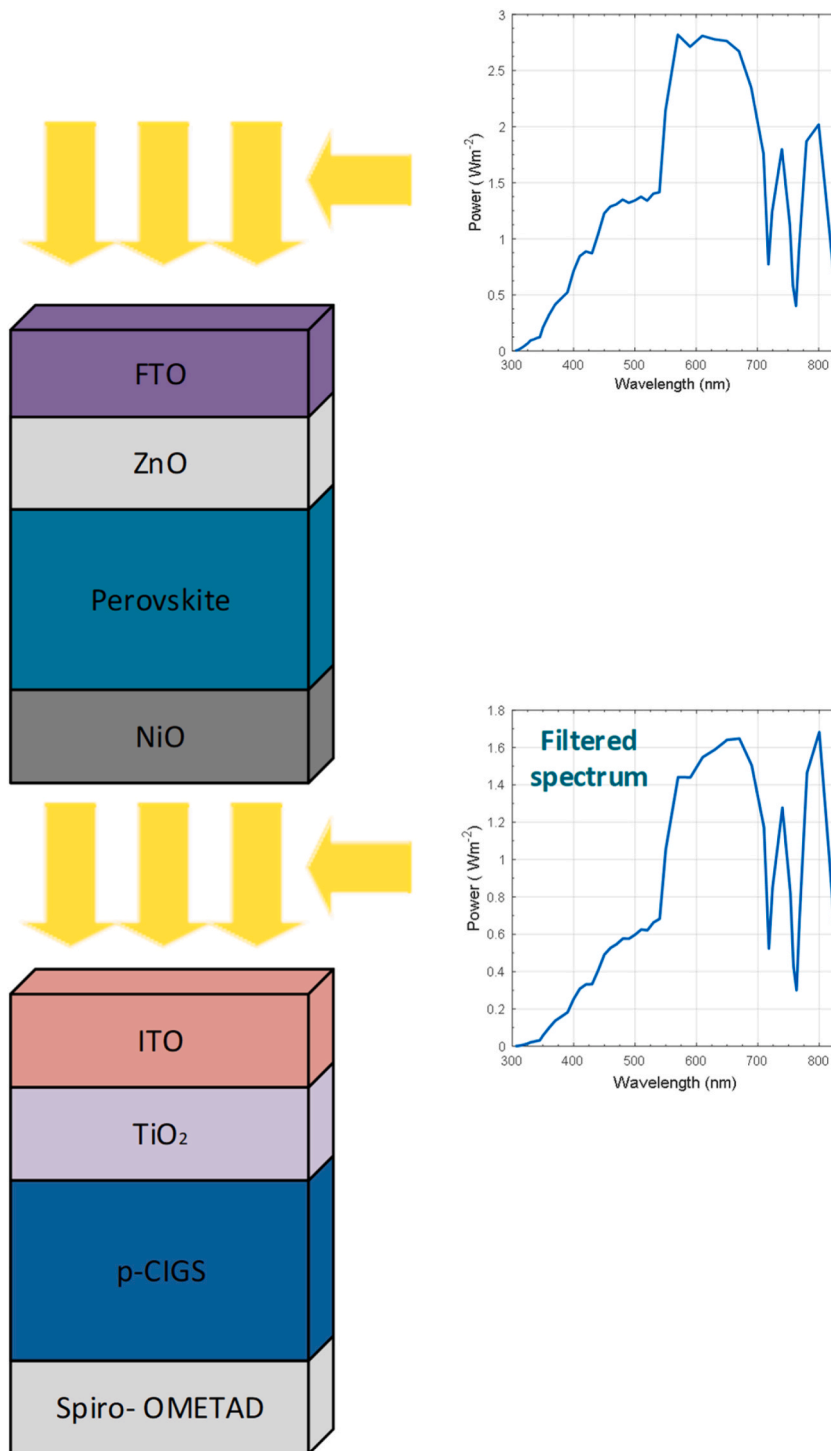
Fig. 11. The proposed tandem cell structure illuminated at standard 1.5G AM spectrum.

sub-cell using the filtered spectrum of solar insolation transmitted via the top cell, the structures were optimized in terms of the thicknesses of the two absorbers to achieve a matched currnt density. It is to be noted that the calculated filtered insolation for various top layer thicknesses is used for current density calculation by varying the bottom layer thickness. For optimum cell performance, the most suitable ETL and HTL materials are also investigated. The thickness of pertinent layers is also optimized to maximize the figure of merits of the proposed tandem solar cell. After synergic optimization with the achievement of desired current matching, the optimum thicknesses of the top and bottom sub-cells are achieved as 198 nm and 1 μm, respectively. The resulting tandem cell attains a
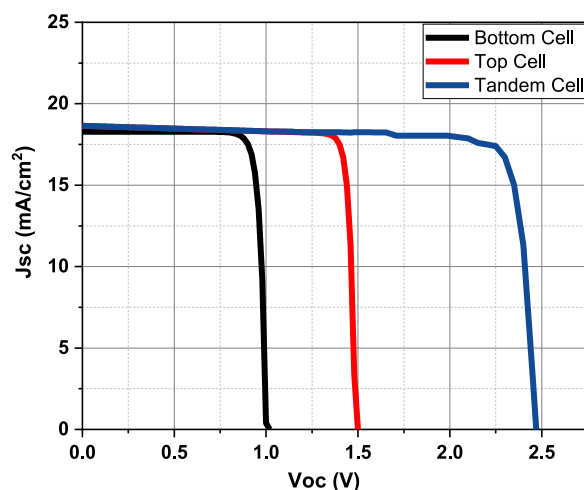
Fig. 12. J-V characteristics of bottom cell, top cell, and the calibrated tandem cell under standard AM1.5G illumination.

Table 3
A summary of the performance characteristics of the designed cells.

Cell	Spectrum	J_{sc} (mA/cm^2)	V_{OC} (V)	FF (%)	PCE (%)
Top cell	AM1.5G	18.64	1.4885	89.077	24.656
Bottom cell	Filtered Spectrum	18.62	1.0006	86.282	25.062
Tandem cell	AM1.5G	18.64	2.48	83.40	38.39

Table 4
Comparison of the proposed tandem cell with existing works.

Ref	Work	Year	Type	Top- bottom cell	Terminal	J_{sc} (mA/cm^2)	V_{OC} (V)	FF (%)	PCE (%)
	This Work	2023	Simulation	Perovskite/CIGS	2-T	18.64	2.48	83.40	38.39
[35]	M. Jošt et al.	2022	Experimental	Perovskite/CIGS	2-T	18.8	1.77	71.2	23.7.
[35]	M. Jošt et al.	2022	Simulation	Perovskite/CIGS	2-T	19.9	2.01	80	32
[54]	A. Kumar et al.	2021	Simulation	Perovskite/CIGS	2-T	17.58	1.646	80.08	23.17
[60]	N. Shrivastav et al.	2023	Simulation	Perovskite/CIGS	2-T	20.04	1.92	77	29.7
[61]	H. Shen et al.	2018	Experimental	Perovskite/CIGS	2-T	–	–	–	23.9
[62]	A. Guchhait et al.	2017	Experimental	Perovskite/CIGS	4-T	–	–	–	20.7
[63]	N. E. I. Boukortt et al.	2023	Simulation	Perovskite/U-CIGS	2-T	20.52	1.705	83.01	29.06

substantial open-circuit voltage of 2.48 V, a short-circuit current density of 18.64 mA cm^{-2}, and an outstanding PCE of 38.39%, surpassing the PCEs of the top and bottom cells, which are 24.656% and 25.062%, respectively. The impacts of defect density and temperature on the performance of both the top and bottom cells are calculated and analyzed. We believe this type of non-toxic perovskite/CIGS tandem solar cell with impressive efficiency and stability will prove as a promising candidate for potential photo-voltaic applications.

Author contribution statement

Md Ashraful Islam: conceived and designed the experiment; performed the experiments.

Atik Jawad: performed the experiments; contributed reagents, materials, analysis tools or data; wrote the paper.

Nahid Akhter Jahan: conceived and designed the experiment; analyzed and interpreted the data; wrote the paper.

M. Mofazzal Hossain: conceived and designed the experiment; analyzed and interpreted the data; contributed reagents, materials, analysis tools or data; wrote the paper

Data availability statement

Data will be made available on request.

Additional information

No additional information is available for this paper.

Declaration of competing interest

The authors declare that they have no known competing financial interests or personal relationships that could have appeared to influence the work reported in this paper.

References

[1] A. Qazi, F. Hussain, N.A. Rahim, G. Hardaker, D.M. Alghazzawi, K.A. Shaban, K. Haruna, Towards sustainable energy: a systematic review of renewable energy sources, technologies, and public opinions, IEEE Access 7 (2019) 63837–63851.

[2] Renewable energy statistics, Irena.org, 2020, https://irena.org/publications/2020/Jul/Renewable-energy-statistics-2020, 2021. (Accessed 10 May 2021).

[3] Marta Victoria, et al., Solar photovoltaics is ready to power a sustainable future, Joule 5 (2021) 1041–1056.

[4] G.F. Nemet, Beyond the learning curve: factors influencing cost reductions in photovoltaics, Energy Pol. 34 (17) (2006) 3218–3232.

[5] M. Mofazzal Hossain, N. Jahan, R.U. Hossain, Simulation and optimization of a highly efficient ZnO/Cu₂O/CdS/CdTe solar cell using SCAPS-1D, 24-26 February 2022, Gazipur, Bangladesh, in: Int. Conf. Advancement in Electrical and Electronic Engineering (ICAEEE), 2022.

[6] N.A. Jahan, M.U. Karim, M.M. Hossain, A high efficiency ultra thin (1.8 μm) CdS/CdTe p-i-n solar cell with CdTe and Si as BSF layer, Adv. Sci. Technol. Eng. Syst. J. 3 (1) (2018) 213–217.

[7] C.S. Solanki, Solar Photovoltaics: Fundamentals, Technologies, and Applications, PHI Learning Pvt. Ltd, 2015.

[8] O. Almora, D. Baran, G.C. Bazan, et al., Device performance of emerging photovoltaic materials (version 3), Adv. Energy Mater. 13 (1) (2022), 2203313.

[9] NREL, Best research-cell efficiency chart. https://www.nrel.gov/pv/assets/pdfs/best-research-cell-efficiencies.pdf.

[10] A. Kojima, K. Teshima, Y. Shirai, T. Miyasaka, Organometal halide perovskites as visible-light sensitizers for photovoltaic cells, J. Am. Chem. Soc. 131 (17) (2009) 6050–6051.

[11] M. Konstantakou, T. Stergiopoulos, A critical review on tin halide perovskite solar cells, J. Mater. Chem. A 5 (23) (2017) 11518–11549.

[12] J. Zhang, G. Hodes, Z. Jin, S. Liu, All-inorganic CsPbX3 perovskite solar cells: progress and prospects, Angew. Chem. Int. Ed. 58 (44) (2019) 15596–15618.

[13] M.K. Hossain, M.K. Mohammed, R. Pandey, A.A. Arnab, M.H.K. Rubel, K.M. Hossain, M.H. Ali, M.F. Rahman, H. Bencherif, J. Madan, M.R. Islam, Numerical analysis in DFT and SCAPS-1D on the influence of different charge transport layers of CsPbBr3 perovskite solar cells, Energy & Fuels 37 (8) (2023) 6078–6098.

[14] M.K. Hossain, G.F. Ishraque Toki, D.P. Samajdar, M.H.K. Rubel, M. Mushtaq, M.R. Islam, M.F. Rahman, S. Bhattarai, H. Bencherif, M.K. Mohammed, R. Pandey, Photovoltaic performance investigation of Cs₃Bi₂I₉-based perovskite solar cells with various charge transport channels using DFT and SCAPS-1D frameworks, Energy & Fuels 37 (10) (2023) 7380–7400.

[15] Q.A. Akkerman, G. Rainò, M.V. Kovalenko, L. Manna, Genesis, challenges and opportunities for colloidal lead halide perovskite nanocrystals, Nat. Mater. 17 (5) (2018) 394–405.

[16] S. De Wolf, J. Holovsky, S.J. Moon, et al., Organometallic halide perovskites: sharp optical absorption edge and its relation to photovoltaic performance, J. Phys. Chem. Lett. 5 (6) (2014) 1035–1039.

[17] S. Senthilarasu, E.F. Fernández, F. Almonacid, T.K. Mallick, Effects of spectral coupling on perovskite solar cells under diverse climatic conditions, Sol. Energy Mater. Sol. Cell. 133 (2015) 92–98.

[18] M.H. Kumar, S. Dharani, W.L. Leong, et al., Lead-free halide perovskite solar cells with high photocurrents realized through vacancy modulation, Adv. Mater. 26 (41) (2014) 7122–7127.

[19] M. Chen, M.G. Ju, H.F. Garces, et al., Highly stable and efficient all-inorganic lead-free perovskite solar cells with native-oxide passivation, Nat. Commun. 10 (1) (2019).

[20] M.K. Hossain, A.A. Arnab, R.C. Das, K.M. Hossain, M.H.K. Rubel, M.F. Rahman, H. Bencherif, M.E. Emetere, M.K. Mohammed, R. Pandey, Combined DFT, SCAPS-1D, and wxAMPS frameworks for design optimization of efficient Cs₂BiAgI₆-based perovskite solar cells with different charge transport layers, RSC advances 12 (54) (2022) 35002–35025.

[21] M. Ikram, R. Malik, R. Raees, M. Imran, F. Wang, S. Ali, M. Khan, Q. Khan, M. Maqbool, Recent advancements and future insight of lead-free non-toxic perovskite solar cells for sustainable and clean energy production: a review, Sustain. Energy Technol. Assessments 53 (2022), 102433.

[22] Y.C. Yong Chan Choi, K.W. Jung, Recent progress in fabrication of antimony/bismuth chalcohalides for lead-free solar cell applications, Nanomaterials 10 (2020) 2284.

[23] M.K. Hossain, D.P. Samajdar, R.C. Das, A.A. A, M.F. Rahman, M.H.K. Rubel, M.K.A. Mohammed, Design and simulation of Cs₂BiAgI₆ double perovskite solar cells with different electron transport layers for efficiency enhancement, Energy Fuels 5 (37) (2023) 3957–3979.

[24] G. Wang, J. Chang, J. Bi, C. Wang, Q. Qiao, Inorganic CsSnI3 perovskite solar cells: the progress and future prospects, Sol. RRL 6 (4) (2022), 2100841.

[25] B. Lee, C.C. Stoumpos, N. Zhou, F. Hao, C. Malliakas, C.Y. Yeh, T.J. Marks, M.G. Kanatzidis, R.P. Chang, Air-stable molecular semiconducting iodosalts for solar cell applications: Cs2SnI₆ as a hole conductor, J. Am. Chem. Soc. 136 (43) (2014) 15379–15385.

[26] P. Xu, S. Chen, H.J. Xiang, X.G. Gong, S.H. Wei, Influence of defects and synthesis conditions on the photovoltaic performance of perovskite semiconductor CsSnI3, Chem. Mater. 26 (20) (2014) 6068–6072.

[27] C. Yu, Z. Chen, J Wang J, W. Pfenninger, N. Vockic, J.T. Kenney, K. Shum, Temperature dependence of the band gap of perovskite semiconductor compound CsSnI3, J. Appl. Phys. 110 (6) (2011).

[28] M.K. Hossain, G.I. Toki, D.P. Samajdar, M. Mushtaq, M.H.K. Rubel, R. Pandey, J. Madan, M.K. Mohammed, M.R. Islam, M.F. Rahman, H. Bencherif, Deep insights into the coupled optoelectronic and photovoltaic analysis of lead-free CsSnI3 perovskite-based solar cell using DFT calculations and SCAPS-1D simulations, ACS Omega 8 (25) (2023) 22466–22485.

[29] X. Qiu, B. Cao, S. Yuan, X. Chen, Z. Qiu, Y. Jiang, Q. Ye, H. Wang, H. Zeng, J. Liu, M.G. Kanatzidis, From unstable CsSnI3 to air-stable Cs₂SnI₆: a lead-free perovskite solar cell light absorber with bandgap of 1.48 eV and high absorption coefficient, Sol. Energy Mater. Sol. Cell. 159 (2017) 227–234.

[30] B. Wu, Y. Zhou, G. Xing, Q. Xu, H.F. Garces, A. Solanki, T.W. Goh, N.P. Padture, T.C. Sum, Long minority-carrier diffusion length and low surface-recombination velocity in inorganic lead-free CsSnI3 perovskite crystal for solar cells, Adv. Funct. Mater. 27 (7) (2017), 1604818.

[31] A. Raj, M. Kumar, H. Bherwani, A. Gupta, A. Anshul, Evidence of improved power conversion efficiency in lead-free CsGeI₃ based perovskite solar cell heterostructure via scaps simulation, J. Vac. Sci. Technol. B 39 (1) (2021) 012401.

[32] M.K. Hossain, G.I. Toki, I. Alam, R. Pandey, D.P. Samajdar, M.F. Rahman, M.R. Islam, M.H.K. Rubel, H. Bencherif, J. Madan, M.K. Mohammed, Numerical simulation and optimization of a CsPbI₃-based perovskite solar cell to enhance the power conversion efficiency, New J. Chem. 47 (10) (2023) 4801–4817.

[33] Md A. Islam, N.A. Jahan, M.M. Hossain, A lead-free all-inorganic Cs2SnI6 based ultra-thin perovskite solar cell optimized using SCAPS-1D simulator, 26-28 October 2022, Pattaya, Thailand, in: 2022 International Conference and Utility Exibition on Energy, Environment and Climate Change (ICUE), 2022.

[34] J. Tong, Q. Jiang, F. Zhang, S.B. Kang, D.H. Kim, K. Zhu, Wide-bandgap metal halide perovskites for tandem solar cells, ACS Energy Lett. 6 (1) (2020) 232–248.

[35] Marko Jošt, et al., Perovskite/CIGS tandem solar cells: from certified 24.2% toward 30% and beyond, ACS Energy Lett. 7 (4) (2022) 1298–1307.

[36] Z. Fang, Q. Zeng, C. Zuo, L. Zhang, H. Xiao, M. Cheng, F. Hao, Q. Bao, L. Zhang, Y. Yuan, W.Q. Wu, Perovskite-based tandem solar cells, Sci. Bull. 66 (6) (2021) 621–636.

[37] Q. Han, Y.-T. Hsieh, L. Meng, J.-L. Wu, P. Sun, E.-P. Yao, S.-Y. Chang, S.-H. Bae, T. Kato, V. Bermudez, Y. Yang, High performance perovskite/Cu(in,Ga)Se$_2$ monolithic tandem solar cells, Science 361 (6405) (2018) 904–908.

[38] A.E. Shalan, S. Narra, T. Oshikiri, K. Ueno, X. Shi, H.-P. Wu, M.M. Elshanawany, E.W.-G. Diau, H. Misawa, Optimization of a compact layer of TiO$_2$ via atomic-layer deposition for high-performance perovskite solar cells, Sustain. Energy Fuels 1 (2017) 1533–1544.

[39] Y. Chen, Q. Meng, L. Zhang, C. Han, H. Gao, Y. Zhang, H. Yan, SnO$_2$-based electron transporting layer materials for perovskite solar cells: a review of recent progress, J. Energy Chem. 35 (2019) 144–167.

[40] L. Lin, T.W. Jones, T.C. Yang, N.W. Duffy, J. Li, L. Zhao, B. Chi, X. Wang, G.J. Wilson, Inorganic electron transport materials in perovskite solar cells, Adv. Funct. Mater. 31 (5) (2021), 2008300.

[41] M.J. Paik, Y. Lee, H.S. Yun, S.U. Lee, S.T. Hong, S.I. Seok, TiO$_2$ colloid-spray coated electron-transporting layers for efficient perovskite solar cells, Adv. Energy Mater. 10 (39) (2020), 2001799.

[42] H. Kato, M. Sano, K. Miyamoto, T. Yao, Growth and characterization of Ga-doped ZnO layers on a-plane sapphire substrates grown by molecular beam epitaxy, J. Cryst. Growth 237 (2002) 538–543.

[43] C. Kuang, G. Tang, T. Jiu, H. Yang, H. Liu, B. Li, W. Luo, X. Li, W. Zhang, F. Lu, J. Fang, Highly efficient electron transport obtained by doping PCBM with graphdiyne in planar-heterojunction perovskite solar cells, Nano Lett. 15 (4) (2015) 2756–2762.

[44] K. Deepthi Jayan, V. Sebastian, Modelling and comparative performance analysis of tin based mixed halide perovskite solar cells with IGZO and CuO as charge transport layers, Int. J. Energy Res. 45 (11) (2021) 16618–16632.

[45] T.K. Tulka, N. Alam, M. Akhtaruzzaman, K. Sobayel, M.M. Hossain, Optimization of a high-performance lead-free cesium-based inorganic perovskite solar cell through numerical approach, Heliyon 8 (11) (2022), e11719.

[46] C. Zuo, L. Ding, Solution-processed Cu$_2$O and CuO as hole transport materials for efficient perovskite solar cells, Small 11 (41) (2015) 5528–5532.

[47] S. Gharibzadeh, B.A. Nejand, A. Moshaii, N. Mohammadian, A.H. Alizadeh, R. Mohammadpour, V. Ahmadi, A. Alizadeh, Two-step physical deposition of a compact CuI Hole-Transport layer and the formation of an interfacial species in perovskite solar cells, ChemSusChem 9 (15) (2016) 1929–1937.

[48] N. Arora, M.I. Dar, A. Hinderhofer, N. Pellet, F. Schreiber, S.M. Zakeeruddin, M. Grätzel, Perovskite solar cells with CuSCN hole extraction layers yield stabilized efficiencies greater than 20, Science 358 (2017) 768–771.

[49] Z. Zhang, S. Chen, P. Li, H. Li, J. Wu, P. Hu, J. Wang, Aerosol-assisted chemical vapor deposition of ultra-thin CuO$_x$ films as hole transport material for planar perovskite solar cells, Functional Materials Letters 11 (2) (2018), 1850035.

[50] M. Shasti, A. Mortezaali, Numerical study of Cu$_2$O, SrCu$_2$O$_2$, and CuAlO$_2$ as hole-transport materials for application in perovskite solar cells, physica status solidi (a) 216 (18) (2019), 1900337.

[51] M. Burgelman, P. Nollet, S. Degrave, Modelling polycrystalline semiconductor solar cells, Thin Solid Films 361–362 (2002) 527–532.

[52] R.A. Jabr, M. Hamad, Y.M. Mohanna, Newton-Raphson solution of Poisson's equation in a pn diode, Int. J. Electr. Eng. Educ. 44 (1) (2007) 23–33.

[53] P. Roy, Y.K. Dongre, S. Tiwari, D. Chaturvedi, A. Khare, Impact of hole transport layer on the performance of all-inorganic tin (Sn) based perovskite solar cells, in: IOP Conference Series: Materials Science and Engineering, IOP Publishing, 2021, March, 012016, 1120(1.

[54] A. Kumar, S. Singh, M.K.A. Mohammed, A.E. Shalan, Computational modelling of two terminal CIGS/perovskite tandem solar cells with power conversion efficiency of 23.1, Eur. J. Inorg. Chem. (47) (2021) 4959–4969.

[55] J. Burdick, T. Glatfelter, Spectral response and I–V measurements of tandem amorphous-silicon alloy solar cells, Sol. Cell. 18 (3–4) (1986) 301–314.

[56] Md Islam, M. Jani, A. Islam, et al., Investigation of CsSn$_{0.5}$Ge$_{0.5}$I$_3$-on-Si tandem solar device utilizing SCAPS simulation, IEEE Trans. Electron. Dev. 99 (2021) 1–8.

[57] J. Madan, Pandey R. Shivani, R. Sharma, Device simulation of 17.3% efficient lead-free all-perovskite tandem solar cell, Sol. Energy 197 (2020) 212–221.

[58] M.H. Jao, H.C. Liao, W.F. Su, Achieving a high fill factor for organic solar cells, J. Mater. Chem. A 4 (16) (2016) 5784–5801.

[59] H. Lu, Y. Ma, B. Gu, W. Tian, L. Li, Identifying the optimum thickness of electron transport layers for highly efficient perovskite planar solar cells, J. Mater. Chem. A 3 (32) (2015) 16445–16452.

[60] N. Shrivastav, S. Kashyap, J. Madan, et al., Perovskite-CIGS monolithic tandem solar cells with 29.7% efficiency: a numerical study, Energy & Fuels 37 (4) (2023) 3083–3090.

[61] H. Shen, T. Duong, J. Peng, et al., Mechanically-stacked perovskite/CIGS tandem solar cells with efficiency of 23.9% and reduced oxygen sensitivity, Energy Environ. Sci. 11 (2) (2018) 394–406.

[62] A. Guchhait, H.A. Dewi, S.W. Leow, et al., Over 20% efficient CIGS–perovskite tandem solar cells, ACS Energy Lett. 2 (4) (2017) 807–812.

[63] N.E.I. Boukortt, S. Patane, A.G. Loureiro, et al., Electrical and optical investigation of 2T–Perovskite/u-CIGS tandem solar cells with ~30% efficiency, IEEE Trans. Electron. Dev. 69 (7) (2022) 3798–3806.